Self-organization of anti-aligning active particles: Waving pattern formation and chaos

Daniel Escaff [ORCID]

Universidad de los Andes, Chile, *Avenida Monseñor Álvaro del Portillo No. 12.455, Las Condes, Santiago, Chile*

Recently, it has been shown that purely anti-aligning interaction between active particles may induce a finite wavelength instability. The formed patterns display intricate spatiotemporal dynamics, suggesting the presence of chaos. Here, we propose a quasi-one-dimensional simplification of the particle interaction model. This simplified model allows us to deduce amplitude equations that describe the collective motion of the active entities. We show that these equations exhibit chaotic orbits. Furthermore, via direct numerical simulations of the particle's system, we discuss the pertinence of these amplitude equations approach for describing the particle's self-coordinated motions.

I. INTRODUCTION

Self-propelled entities may display a vast range of self-coordinated motions, from the flocking transition, where the particles move in unison, to more complex flocks.

Since the pioneering work of Vicsek *et al.* [1], the topic of flocking transition has attracted much attention. Even though Vicsek's model is simple for numerical studies, it is complicated for analytical investigations. Consequently, during the 2000s decade, there was much debate about the nature of the flocking transition: Is it a first- or second-order transition? [2] More recently, it has been shown that Vicsek's model exhibits a transition to flocking with many of the features of a liquid-gas transition as a spinodal decomposition [3]. Today, Vicsek's model has also been analyzed within the framework of kinetic theory, where hydrodynamic equations can be obtained via the Chapman-Enskog expansion [4], as well as using the tools of bifurcation theory [5].

Besides Vicsek's model, many alternative approaches to the flocking phenomena exist. For example, active Brownian particles [6] have attracted growing attention. Moreover, flocking phenomena are a type of synchronization of such particles. Then, Kuramoto-like [7] approaches may also be appropriate. In fact, Chepizhko and Kulinskii [8] pointed out the similarities between the Kuramoto model and the previous hydrodynamics model proposed by Kulinskii *et al.* [9], namely, they showed that the polar angle of the velocity obeys a similar (but not identical) equation of motion to the phase of oscillation in Kuramoto's model. In addition, they compared a noisy version of Kulinskii's model with the Kuramoto model for oscillators with randomly distributed frequencies, showing that they exhibit a similar bifurcation structure for different kinds of randomness [10]. Then, Sevilla *et al.* used a quite similar velocity-aligning force to show that simple Brownian particles (non-self-propelled particles, which are just driven by environmental fluctuations) can also exhibit collective motion due to this kind of interaction [11]. In 2012, Farrell *et al.* studied a generalization of the Kuramoto model for active units (which is presented by them as a continuous time variant of Vicsek's model); due to the inclusion of a density-dependence velocity

of the self-propelled agents, they observed a quite interesting pattern-forming process [12]. Furthermore, Levis *et al.* showed that, by considering motile Kuramoto-type oscillators with randomly distributed frequencies, they observed a long-range synchronization in two spatial dimensions, even for short-range interaction (which is precluded for motionless oscillators in two dimensions) [13]. Moreover, they reported an opposite chirality particle cooperation, analyzing the system using a hydrodynamics approach, which is valid for short-range interaction (see also Ref. [14] for a deep mathematical foundation of this hydrodynamics approach). In addition, the appearance of self-propelled chimeras has also been reported [15]. A phase shift in the Kuramoto-like interaction term must be included to observe these self-propelled chimeras; hence, the interaction does not promote a perfect alignment. More recently, Negi *et al.* used this kind of approach to include visual perception in the active agents [16]. Furthermore, the topic of swarmalators, where self-propulsion and oscillations are independent but coupled degrees of freedom, has become a growing field [17].

Aligning Kuramoto-type interactions leads to a synchronized movement, where the active particles move in the same direction. The flocking transition is a first-order transition for small interaction ranges (and is related to cluster formation) and is a second-order transition for larger interaction ranges (and is related to the formation of a spatially uniform flux) [18]. It is worth mentioning that the phase diagram of this model is remarkably similar to the one observed in a one-dimensional flocking model based on the persistent-random-walk paradigm [19] (noting that persistent-random-walk-like transport behaviors of active suspensions have been widely documented [20]). The transition is related to an infinite wavelength (or zero wave number) instability [12,18,19]. Conservative generalizations of this type of aligning forces may induce a finite wavelength instability [18]. In the last case, which involves cohesive forces, the transition is highly subcritical; after a spinodal decomposition, the active particles form a single self-propelled cluster. Moreover, apolar generalizations of this type of interaction lead to the formation of two counterpropagating clusters [21]. These clusters

024603-1

interact as dissipative solitons; namely, they interact by exhibiting two of the four classical behaviors of counter-propagating dissipative solitons [22]: they interpenetrate and continue their movement after colliding or forming a bound state where the clusters remain together.

Recently, it has been shown that purely anti-aligning interaction induces a finite wavelength instability [23], namely, a negative coupling strange in the Kuramoto-like interaction term induces a nonzero wave-number instability that leads to pattern formation. Moreover, the same phenomenon is observed in Vicsek's model with anti-aligning coupling [23]. It is worth mentioning that Bonilla and Trenado previously included anti-alignments as fluctuations in Vicsek's model [24]. They observed a zero wave-number Hopf-type instability leading to oscillatory flockings. Furthermore, Großmann *et al.* showed that selective attraction-repulsion interaction (short-range alignment and large-range anti-alignment) may induce a wide variety of patterns, including vortex arrays and mesoscale turbulence [25]. Beyond the topic of active matter, antisynchronous interaction leading to oscillatory patterns has been documented, for example, in populations of globally coupled Kuramoto oscillators [26] and lattices of three-state-stochastic oscillators [27].

Due to the finite wavelength instability reported in Ref. [23], the system displays a pattern-forming process. The formed pattern may exhibit a pretty intricate spatiotemporal dynamics, which involves, let us say, some choreographic movement of the active entities. The active particles self-synchronize, forming two counterpropagating hexagonal traveling waves. They are assembling and disassembling a global hexagonal structure and a striped lineup of particles. Since these hexagonal waves seem to be performing some kind of dance, we called them the *dancing hexagons*. The dance steps become quite erratic for long-time simulations, suggesting the presence of chaos.

Here, we present a quasi-one-dimensional simplification of the Kuramota-like model presented in Ref. [23]. To wit, we confine the particles in a thin channel. In Sec. II, we present the model, showing that it undergoes a finite wavelength instability, leading to a longitudinal density wave formation. We perform a weakly nonlinear analysis in Sec. III, that is, neglecting the system's fluctuations near the critical point, and for low speed, we deduce a set of amplitude equations for describing the wave dynamics. Then, we show that these equations have chaotic orbits. Moreover, in Sec. IV, we compare the amplitude equations' predictions with direct numerical simulations of the particles' system, discussing the agreements and discrepancies. Finally, in Sec. V, we summarize our findings and present our conclusions.

II. QUASI-ONE-DIMENSIONAL SIMPLIFIED MODEL

A. Particles in a channel

Let us consider a set of N active particles that are confined in a channel. More precisely, a set of particles which are characterized by their positions $\{\vec{r}_l = (x_l, y_l)\}_{l=1}^{N}$ and the orientation angles $\{\theta_l\}_{l=1}^{N}$. They are confined in a rectangular domain of dimensions $L_x > L_y$, as illustrated in the Fig. 1.
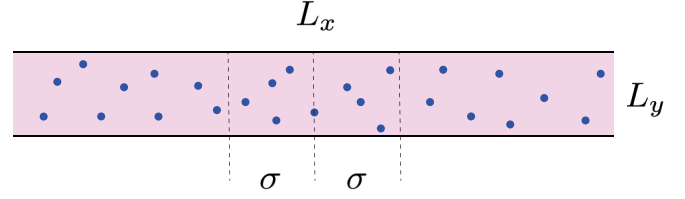

FIG. 1. Schematic drawing of active particles confined in a channel.

Each particle moves with a constant speed v in the direction $\hat{\theta}_l = (\cos\theta_l, \sin\theta_l)$ and obeys the equations of motion

$$\dot{\vec{r}}_l = v\hat{\theta}_l, \tag{1}$$

$$\dot{\theta}_l = \frac{\bar{a}}{2\sigma L_y} \sum_{\vec{r}_j \in \mathcal{D}_\sigma(\vec{r}_l)} \sin(\theta_j - \theta_l) + \sqrt{\eta}\,\xi_l(t), \tag{2}$$

where $\mathcal{D}_\sigma(\vec{r})$ represents the interaction domain. Reference [23] considers a circular interaction domain; here we will assume that the particles only interact along the channel (see Fig. 1) due to

$$\vec{r}\,' \in \mathcal{D}_\sigma(\vec{r}) \text{ if } |x - x'| < \sigma.$$

It may be compatible with a circular domain if the channel is considerably thinner than the interaction range ($L_y \ll \sigma$). On the other hand, $\xi_l(t)$ are independent Gaussian white noises, $\langle\xi_l(t)\rangle = 0$ and $\langle\xi_j(t')\xi_l(t)\rangle = \delta_{jl}\delta(t' - t)$. η is the noise intensity. The parameter $\bar{a}$ is related to the coupling strength, normalized by the area of the interaction domain.

Furthermore, since the interaction range does not depend on the traversal position, $\{y_l\}_{l=1}^{N}$ only affect the particles' polarizations when colliding with the channel borders. Considering, then, periodic boundary conditions, Eqs. (1) and (2) may be reduced to the autonomous quasi-one-dimensional system

$$\dot{x}_l = v\cos\theta_l, \tag{3}$$

$$\dot{\theta}_l = \frac{a}{2\sigma} \sum_{|x_j - x_l| < \sigma} \sin(\theta_j - \theta_l) + \sqrt{\eta}\,\xi_l(t), \tag{4}$$

where $a = \bar{a}/L_y$. Notice that model equations (3) and (4) can be directly related to the model presented in Ref. [23] if we drastically decrease one of the two dimensions. Although taking null-flux boundary conditions along the transversal direction seems more realistic, there are no significant differences for the purposes of this report. As shown below, the unstable Fourier modes along the longitudinal direction rule the pattern-forming process. Then, for the sake of simplicity, we will focus on the equations of motion (3) and (4).

Aligning interactions are related to $a > 0$ while anti-alignments with $a < 0$ [23].

At the macroscopic level, the system may be described by the particle density

$$\mathcal{N}(x, \theta, t) = \sum_{l=1}^{N} \delta(x_l(t) - x)\delta(\theta_l(t) - \theta). \tag{5}$$

Neglecting the inherent fluctuations of a finite N ensemble (which typically scales as $\sqrt{N}$), this density can be

approached by its mean value $NP(\theta, x, t)$, where P corresponds to the one-particle probability distribution. At this level of approximation, P satisfies the nonlinear Fokker-Planck equation

$$\partial_t P = -v \cos \theta \, \partial_x P + \frac{\eta}{2} \partial_\theta^2 P - \partial_\theta [P \mathcal{T}_x P], \quad (6)$$

where

$$\mathcal{T}_x P = \frac{Na}{2\sigma L_y} \int_{x-\sigma}^{x+\sigma} dx' \int_0^{2\pi} d\theta' P(\theta', x', t) \sin(\theta' - \theta).$$

B. Finite wavelength instability and waving pattern formation

The asynchronous state is represented by the uniform distribution

$$P = \frac{1}{2\pi L_x}.$$

Introducing a perturbation in the Fourier space,

$$P(\theta, x, t) = \frac{1}{2\pi L_x} + \bar{\epsilon} \exp{(\lambda(k)t + ikx)} \Phi(\theta),$$

and linearizing respect to the small perturbation parameter $\bar{\epsilon}$, an eigenvalues problem is obtained to compute the $\lambda(k)$ spectrum [18,23]:

$$(\mathcal{L}_0 - ivk\mathcal{L}_1)\Phi = \lambda(k)\Phi. \quad (7)$$

$\mathcal{L}_0$ is diagonal in the basis $\{e^{im\theta}\}_{m=-\infty}^{\infty}$,

$$\mathcal{L}_0 e^{im\theta} = \lambda_m^{[0]}(k) e^{im\theta},$$

with the eigenvalues

$$\lambda_m^{[0]}(k) = -\frac{\eta}{2}m^2 + \frac{v_0 a}{2} \left(\frac{\sin{(k\sigma)}}{k\sigma} \right) (\delta_{m,1} + \delta_{m,-1}), \quad (8)$$

where $v_0 = N/L_x$ is the global density, while

$$\mathcal{L}_1 e^{im\theta} = (e^{i(m+1)\theta} + e^{i(m-1)\theta})/2.$$

Furthermore, the periodic boundary condition demands

$$k = \frac{2\pi n}{L_x},$$

with n an integer.

Therefore, the asynchronous state is stable only if

$$\forall n \quad \mathrm{Re} \left[\lambda \left(\frac{2\pi n}{L_x} \right) \right] < 0,$$

otherwise it is unstable. Finite wavelength instabilities are related to $n \neq 0$.

1. Without self-propulsion

For $v = 0$, the particles do not move. It is like a disordered lattice. The $\lambda(k)$ spectrum corresponds to $\lambda_m^{[0]}(k)$, i.e., Eq. (8). The asynchronous state becomes unstable at the critical point

$$v_0 a_c \left(\frac{\sin{(2\pi n_c \sigma/L_x)}}{2\pi n_c \sigma/L_x \sigma} \right) = \eta, \quad (9)$$

$$v_0 a_c \left(\frac{\sin{(2\pi n \sigma/L_x)}}{2\pi n \sigma/L_x \sigma} \right) < \eta \quad \forall n \neq n_c. \quad (10)$$

These conditions relate the critical coupling strength a_c with the critical wave number n_c.
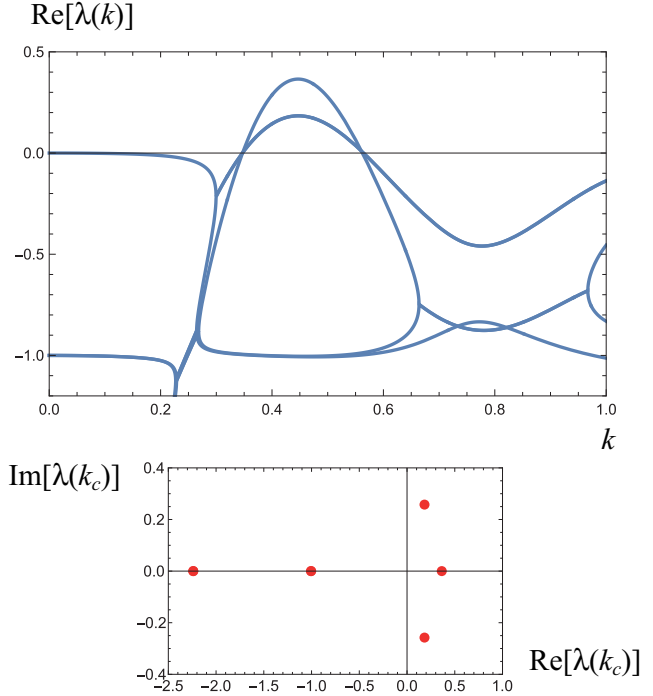

FIG. 2. Numerical computation of the $\lambda(k)$ spectrum in the truncated basis $\{e^{im\theta}\}_{m=-10}^{10}$ with $v/L_x = 0.01$, $v_0 a = -6$, $\sigma/L_x = 0.1$, and $\eta = 0.5$. Top: $\mathrm{Re}[\lambda(k)]$ versus k. Bottom: Eigenvalues at the critical wave number $k_c = 2\pi n_c/L_x$, where $n_c = 7$ for $L_x = 100$ ($\sigma = 10$).

Notice that, in this speedless case, the only modes that are excited during the instability have $m = \pm 1$. As pointed out in Ref. [23], spatial structuring is related to the excitation of the mode $m = 0$ (see also the discussion below).

For aligning interaction $a > 0$, the critical wave number is $n_c = 0$ ($v_0 a_c = \eta$), leading to a global alignment of the particles.

In contrast, anti-aligning interaction $a < 0$ induces a finite wavelength instability ($n_c \neq 0$), leading to the formation of a static polarization pattern [23].

2. With self-propulsion

Here we have solved the eigenvalues problem (7) in the truncated basis $\{e^{im\theta}\}_{m=-M}^{M}$. Figure 2 shows one of our results. In this case, the instability involves the confluence of three modes: two of them with a non-null imaginary part (see the bottom panel of Fig. 2). Therefore, it corresponds to a type I_o instability in the Cross-Hohenberg classification [28] (an oscillatory finite wavelength instability).

In contrast with the speedless case, this instability involves a strong excitation of the mode $m = 0$. Reference [23] has a detailed analysis of this linear stability problem. In fact, as Appendix A shows, the linear problem for the dimensional-reduced model has the same structure as in the two-dimensional case [23,29]. The resulting pattern of the quasi-one-dimensional dynamics is a standing wave, as shown in Fig. 3. More precisely, Fig. 3 displays a spatiotemporal
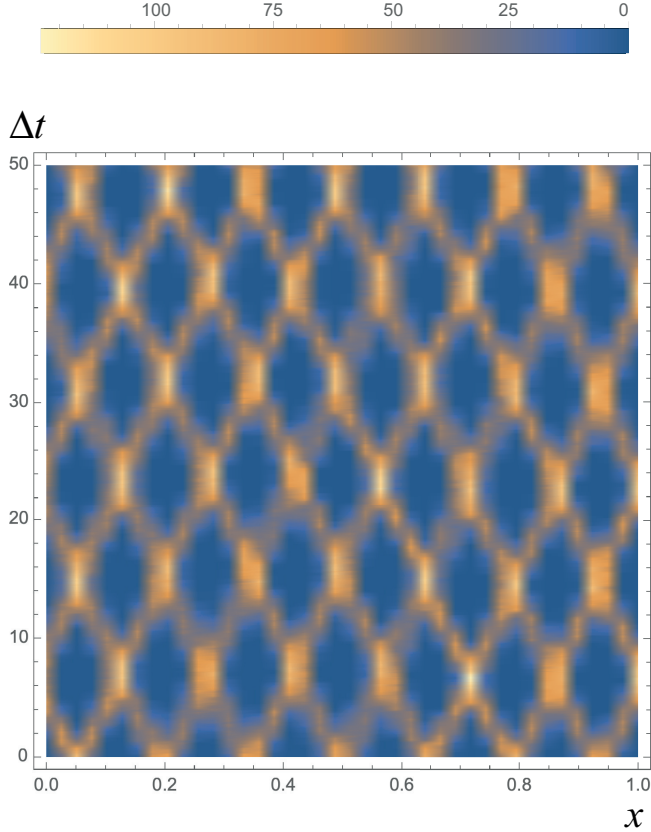
FIG. 3. Numerical simulation of the equations of motion (3) and (4) for $v = 0.01$, $v_0 a = -6$, $\sigma = 0.1$, $\eta = 0.5$, $N = 1000$, $L_x = 1$, and $dt = 0.05$ (using an Euler-Maruyama method). We are showing the spatiotemporal diagram of $\chi_\Delta(x, t)$, as defined in Eq. (11), with $\Delta = 0.025$.

diagram of the coarse-grained spatial density:

$$\chi_\Delta(x, t) = \int_{x-\Delta/2}^{x+\Delta/2} dx' \int_0^{2\pi} \mathcal{N}(x', \theta, t) d\theta. \quad (11)$$

The underlying dynamics of this standing wave consists of two counterpropagating traveling waves. In some sense, it is making a one-dimensional mimic of the dancing waves. As we will see below, this apparently simple wave dynamics also hides complex features.

C. Pattern-forming dynamics

In summary, motionless particles lead to the formation of a static polarization pattern. This might be seen as an equilibriumlike antiferromagnetic state (if the magnetic analogy applies). The system is then driven out of this equilibriumlike state by self-propulsion. As a consequence of that, the new nonequilibrium steady state displays permanent spatiotemporal dynamics.

It is worth noting that, expanding

$$P(\theta, x, t) = \sum_{m=-\infty}^{\infty} g_m(x, t) e^{im\theta},$$

and neglecting the fluctuations, we may approach

$$\chi_\Delta(x, t) \approx \Delta N g_0(x, t).$$

Therefore, the dynamics of the density wave is ruled by the dynamics of the mode $m = 0$.

As we will see in the next section, the weakly nonlinear analysis near the critical point (and for low speed) predicts:

(1) Without self-propulsion: A potential relaxation dynamics for the modes $m = \pm 1$ related to the unstable wave number. Leading to a static steady state, without excitations of the mode $m = 0$.

(2) With self-propulsion: A nonpotential dynamics leading to a permanent movement. In particular,

$$g_0(x, t) \approx \mathrm{Re}[A_0(t) e^{ik_c x}]/\pi L_x,$$

where $A_0(t)$ oscillates chaotically.

III. WEAKLY NONLINEAR ANALYSIS

A. Perturbative scheme and amplitude equations

The full derivation of the amplitude equations can be found in Appendix A. Here we summarize the main results.

Near criticality, and for small v, the probability $P(\theta, x, t)$ may be approached by

$$P(\theta, x, t) \approx \frac{1}{2\pi L_x}(1 + 2\mathrm{Re}[(A_+ e^{i\theta} + A_0 + A_- e^{-i\theta}) e^{ik_c x}]), \quad (12)$$

where A_+, A_0, and A_- are the amplitudes of the unstable modes, at least for small v, and

$$k_c = \frac{2\pi n_c}{L_x}.$$

To capture the nonlinear evolution of these amplitudes near criticality ($a \sim a_c$), we have assumed the perturbative scheme

$$v \sim v_0(a_c - a),$$
$$A_+ \sim A_0 \sim A_- \sim \sqrt{v_0|a_c - a|},$$
$$\dot{A}_+ \sim \dot{A}_0 \sim \dot{A}_- \sim (v_0|a_c - a|)^{3/2},$$

which is the standard scaling of a pitchfork bifurcation. Note that since we are taking the speed v perturbatively, the value of a_c corresponds to the one predicted by Eq. (9).

Thus, it is expected that these amplitudes obey the equations

$$\dot{A}_+ = \varepsilon A_+ + i\Omega A_0 - c_1 A_0^2 A_-^* - c_2|A_0|^2 A_+ - c_3(2|A_-|^2 + |A_+|^2)A_+, \quad (13)$$

$$\dot{A}_0 = i\Omega(A_+ + A_-), \quad (14)$$

$$\dot{A}_- = \varepsilon A_- + i\Omega A_0 - c_1 A_0^2 A_+^* - c_2|A_0|^2 A_- - c_3(2|A_+|^2 + |A_-|^2)A_-, \quad (15)$$

where

$$\varepsilon = \frac{\eta(a - a_c)}{2a_c}, \quad \Omega = \frac{k_c v}{2}, \quad (16)$$

and the coefficients c_1, c_2, and c_3 are positive real numbers. The exact expression of these coefficients can be found in Appendix A.

B. Without self-propulsion

For $v = 0$ ($\Omega = 0$), A_0 remains at rest. Starting with a random distribution of particles, $A_0 = 0$ during the whole system evolution. Hence, the amplitude equations reduce to the potential system

$$\dot{A}_\pm = -\frac{\partial \mathcal{U}}{\partial A_\pm^*},$$

where

$$\mathcal{U} = -\varepsilon(|A_-|^2 + |A_+|^2) + c_3\left[\tfrac{1}{2}(|A_-|^4 + |A_+|^4) + 2|A_-|^2|A_+|^2\right]. \quad (17)$$

Thus, it is a relaxation dynamics that minimizes the potential (17). Therefore, all the steady-state amplitudes are static and correspond to minima (stable solutions), maxima (unstable solutions), or saddle points (unstable solutions) of the potential (17). In general, we may write these solutions as

$$A_\pm = R_\pm e^{i\varphi_\pm},$$

where $\varphi_\pm$ are arbitrary phases.

The asynchronous state

$$R_- = R_+ = 0, \quad (18)$$

is stable when $\varepsilon < 0$ [minimum of (17)] and unstable when $\varepsilon > 0$ [maximum of (17)], as expected. Besides, above the critical point ($\varepsilon > 0$), there are the solutions

$$R_\pm = \sqrt{\frac{\varepsilon}{c_3}} \quad \text{and} \quad R_\mp = 0, \quad (19)$$

which is stable [minimum of (17)], and the saddle point of (17) (that is, the unstable solution)

$$R_- = R_+ = \sqrt{\frac{\varepsilon}{3c_3}}. \quad (20)$$

C. With self-propulsion

1. Static solutions

Considering the particle's self-propulsion ($v \neq 0$), only two of the three static solutions we found for the speedless case remain. The asynchronous state, where the linear stability analysis gives the eigenvalues

$$\Lambda_1 = \varepsilon,$$

$$\Lambda_\pm = \frac{\varepsilon}{2} \pm i\sqrt{2\Omega^2 - \left(\frac{\varepsilon}{2}\right)^2}.$$

Here, again, the asynchronous state is stable when $\varepsilon < 0$ and unstable when $\varepsilon > 0$. However, in this case, the instability takes place with the oscillatory frequency $\omega = \sqrt{2}\Omega$; that is, it is a Hopf-type of instability. Moreover, it is worth noting that this result coincides with the perturbative analysis performed in Ref. [23].

The other static solution is

$$A_+ = -A_- = \sqrt{\frac{\varepsilon}{3c_3}}e^{i\varphi} \quad \text{and} \quad A_0 = 0, \quad (21)$$

where φ is an arbitrary phase. Therefore, it corresponds to the solution (20) with the constraint

$$\varphi_+ - \varphi_- = \pm\pi. \quad (22)$$

Of course, it is unstable. The linear stability analysis leads to the eigenvalues

$$\Lambda \in \left\{ -2\varepsilon, \frac{\varepsilon}{3} \pm i\sqrt{2\Omega^2 - \left(\frac{\varepsilon}{3}\right)^2}, 0, \pm i\sqrt{2}\Omega \right\}.$$

Therefore, this static solution borns unstable at $\varepsilon = 0$ and exists for $\varepsilon > 0$. Here, again, a small perturbation involves oscillatory frequencies.

2. Unstable limit cycles

Defining

$$A_\pm = Z_\pm e^{i\varphi} \quad \text{and} \quad A_0 = Z_0 e^{i\varphi}$$

with φ an arbitrary phase, and separating real and imaginary parts

$$Z_\pm = X_\pm + iY_\pm \quad \text{and} \quad Z_0 = X_0 + iY_0,$$

we may introduce the variables

$$V = X_+ - X_- \quad \text{and} \quad W = X_+ + X_-.$$

Then, if we take the initial condition,

$$Y_\pm(t=0) = X_0(t=0) = V(t=0) = 0, \quad (23)$$

these variables will remain null during the whole system evolution. Hence, the amplitude equations (13)–(15) reduce to the bidimensional system

$$\dot{W} = \varepsilon W + 2\Omega Y_0 - \left(\bar{c}_2 Y_0^2 + \bar{c}_3 W^2\right)W, \quad (24)$$

$$\dot{Y}_0 = -\Omega W, \quad (25)$$

where $\bar{c}_2 = c_2 - c_1$ and $\bar{c}_3 = 3c_3/4$.

The fixed point $(W, Y_0) = (0, 0)$ corresponds to the asynchronous state and has the eigenvalues $\Lambda_\pm$. Therefore, the dynamical system (24) and (25) undergoes a Hopf bifurcation at $\varepsilon = 0$, giving rise to the formation of a limit cycle.

Since we introduced the arbitrary phase φ, they form, in fact, a continuous family of limit cycles. Moreover, the same dynamical system is obtained by considering the pair $W' = Y_+ + Y_-$ and X_0.

These limit cycles are unstable under perturbations of the initial condition (23).

3. Attractive orbits

Let us focus on the complex plane of the mode $m = 0$ amplitude (see Appendix B for a discussion of the modes $m = \pm 1$ amplitudes). Figures 4 and 5 show attractors of Eqs. (13)–(15). They are open orbits that never close.

These attractive orbits are circular-shaped near the critical point ($v_0 a_c \cong -2.312$), as shown in Fig. 4. In contrast, getting away from criticality, they become more elongated, as shown in Fig. 5. The bone-shaped formations may have an arbitrary orientation according to phase invariance.
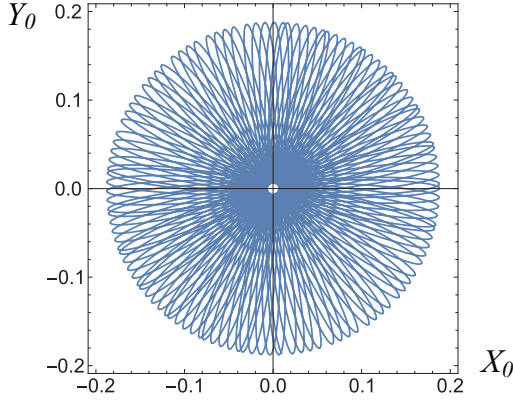
FIG. 4. Numerical simulation of the amplitude equations (13)–(15) [30] for $v_0 a = -2.5$, $v/L_x = 0.001$, $\eta = 0.5$, and $\sigma/L_x = 0.1$ [see Eqs. (16) and (A2)–(A4)]. After a transient, we show the attractor in time window $t \in [5.8 \times 10^4, 7 \times 10^4]$.

We have computed the maximum Lyapunov exponent to check the susceptibility of these attractors to the initial conditions, namely, defining

$$\vec{q} = (X_+, Y_+, X_0, Y_0, X_-, Y_-),$$

we may write the amplitude equations (13)–(15) as

$$\dot{\vec{q}} = \vec{F}(\vec{q}).$$

Let $\vec{q}(t) = \vec{\zeta}(t)$ be an attractor of this system. Then, we define

$$f(t) = \ln\left(\frac{|\delta\vec{q}(t)|}{|\delta\vec{q}(0)|}\right) \quad \text{with} \quad \dot{\delta\vec{q}} = DF[\vec{\zeta}(t)]\delta\vec{q}, \qquad (26)$$

where $DF[\vec{\zeta}(t)]$ is the Jacobian matrix of $\vec{F}$ evaluated in the attractive orbit $\vec{\zeta}(t)$, and $\delta\vec{q}$ is a vector relates to a small perturbation of this orbit. Hence, the maximum Lyapunov exponent corresponds to

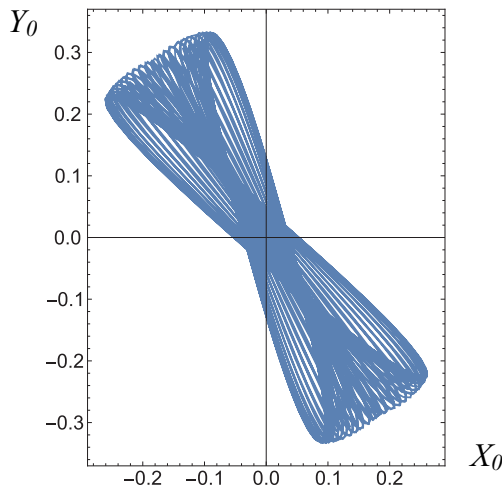$$\lambda_{\max} = \lim_{t\to\infty} \frac{f(t)}{t}.$$

FIG. 5. Same as Fig. 4, except that $v_0 a = -3$ and $t \in [3 \times 10^4, 5 \times 10^4]$.
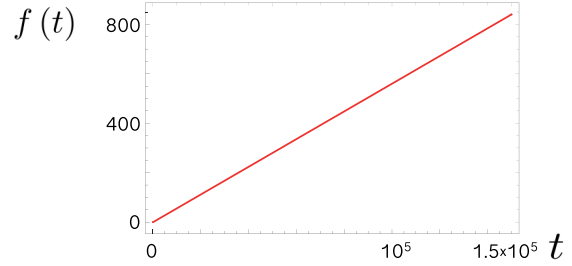

FIG. 6. Numerical estimation of the function $f(t)$, as defined in Eq. (26), for the attractor $\vec{\zeta}(t)$ shown in Fig. 4. More precisely, we take the last state of Fig. 4 as the initial condition, run it for a time $t = 1.5 \times 10^5$, and use it to construct the Jacobian matrix. Then, we solve the linear system related to this matrix using an Euler method with $dt = 0.1$.

Figure 6 shows our computation of $f(t)$ for the attractor $\vec{\zeta}(t)$ shown in Fig. 4. The maximum Lyapunov exponent can be estimated $\lambda_{\max} \approx 0.0056$, which is positive. Even though it is small, the exponential divergence is clear from Fig. 6. For the attractor shown in Fig. 5, we obtained $\lambda_{\max} \approx 0.0215$. Therefore, despite the apparent regularity of these orbits, they are chaotic.

The sensibility to initial conditions becomes clearer if we take the perturbation $\vec{\zeta} + \delta\vec{q}$ and, instead of linearizing, we leave it to evolve following the full nonlinear dynamics dictated by the amplitude equations (13)–(15). Figure 7 displays one of these experiments for the attractor $\vec{\zeta}(t)$ shown in Fig. 4. A small perturbation shows a quite divergent dynamics. After the turbulent transient, the system reestablishes the attractor. Figure 8 shows the same experiment for the the attractor $\vec{\zeta}(t)$ shown in Fig. 5. The dynamics becomes quite erratic again, with a turbulent and divergent transient ending in the attractor's reestablishment with a different orientation, as expected from the phase invariance.

For the parameters explored here, these are the typical observed dynamics. Below the critical point, the only attractor is the asynchronous state (with $A_0 = A_\pm = 0$). An attractive open orbit (with a positive maximum Lyapunov exponent) supercritically appears at the critical point. These attractors may draw a circular-shaped figure in the A_0 plane (nearly above the critical point) or a more elongated one (moving away from the critical point). In Appendix B, we give more details about these orbits, in particular, the behaviors of the amplitudes $A_\pm$.

IV. NUMERICAL OBSERVATIONS

Notice that

$$A_0 = \int_0^{2\pi} d\theta \int_0^{L_x} dx\, P(\theta, x, t)e^{-ik_c x},$$

$$A_\pm = \int_0^{2\pi} d\theta \int_0^{L_x} dx\, P(\theta, x, t)e^{-i(k_c x \pm \theta)}.$$

Then, approaching (that is, neglecting noisy fluctuations)

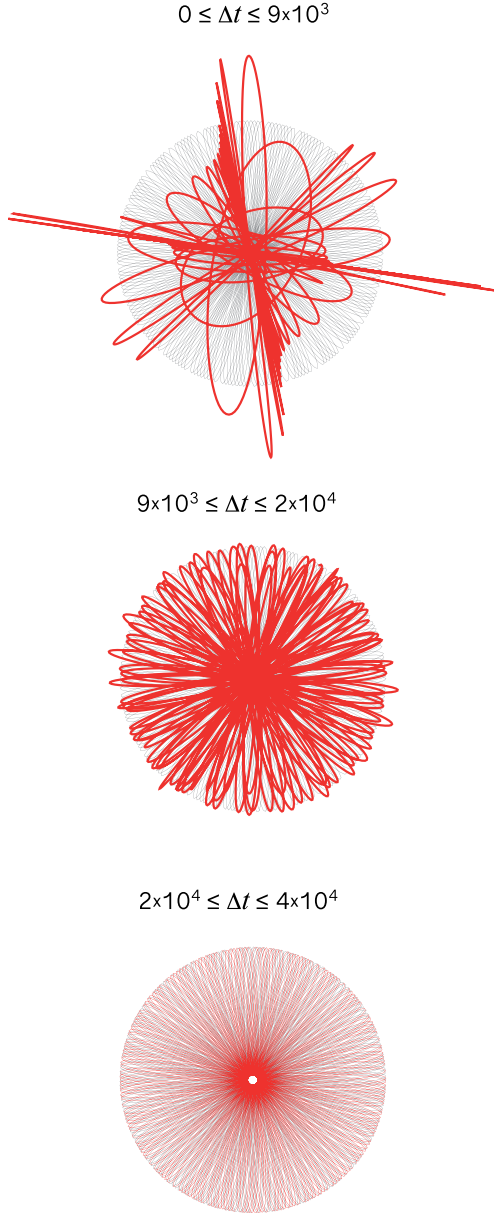$$P(\theta, x, t) \approx \frac{\mathcal{N}(x, \theta, t)}{N},$$

FIG. 7. Numerical simulation of the amplitude equations (13)–(15) [30] for the same parameters as Fig. 4. We have omitted the axes because the orbits have the same dimensions as Fig. 4. The background orbit (thinner trajectory) is the attractor $\vec{\zeta}(t)$ shown in Fig. 4. The thicker trajectory corresponds to the nonlinear evolution of the perturbation $\vec{\zeta}(t_0) + \delta\vec{q}$, where $\delta\vec{q} = (10^{-5}, 0, 0, -7 \times 10^{-5}, 0, 9 \times 10^{-7})$. The different panels display different time windows, showing at the top of each orbit, where $\Delta t = t - t_0$.

where the density $\mathcal{N}$ is defined in Eq. (5), we may define the empirical amplitudes

$$\mathcal{A}_0 = \frac{1}{N} \sum_{j=0}^{N} e^{-ik_c x_j}, \tag{27}$$

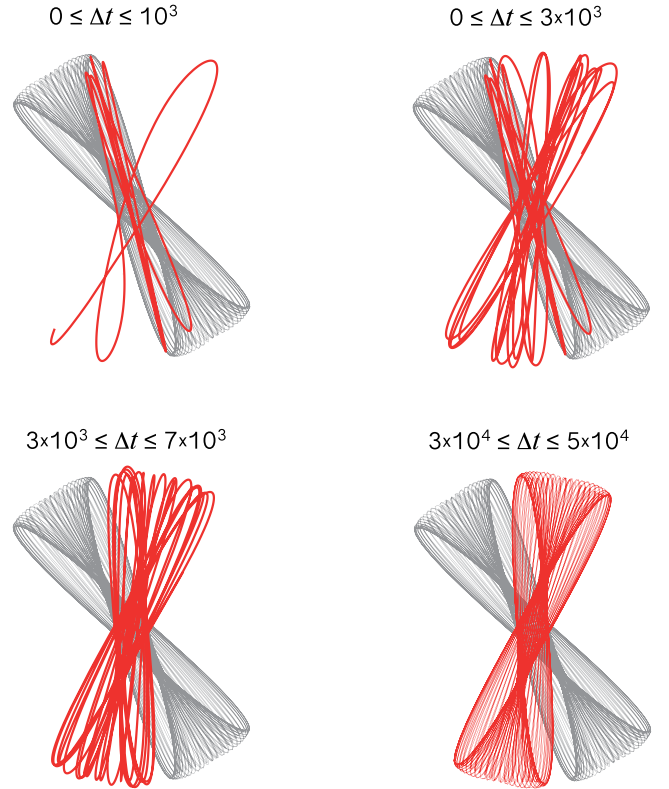$$\mathcal{A}_\pm = \frac{1}{N} \sum_{j=0}^{N} e^{-i(k_c x_j \pm \theta_j)}. \tag{28}$$

FIG. 8. As in Fig. 7, but for the attractor and parameters shown in Fig. 5. $\delta\vec{q} = (10^{-3}, 0, -10^{-3}, 0, 0, 7 \times 10^{-5})$.

And separate real and imaginary parts:

$$\mathcal{A}_0 = \mathcal{X}_0 + i\mathcal{Y}_0 \quad \text{and} \quad \mathcal{A}_\pm = \mathcal{X}_\pm + i\mathcal{Y}_\pm.$$

A. Mode $m = 0$ amplitude

Figure 9 displays $\mathcal{A}_0$ planes from numerical simulations of the simplified model (3) and (4). As the amplitude equations predict, the orbits tend to draw a more circular formation near the critical point. Of course, since noise is unavoidable in the particles' system dynamics, these orbits seem to be in a perpetual transient where they display the most turbulent aspects of their dynamics (see, for instance, upper panel of Fig. 7). As we move away from the critical point, the orbits display a more elongated figure in the $\mathcal{A}_0$ plane, in concordance, again, with the amplitude equations predictions.

Furthermore, the elongated formation is also expected to destabilize, changing its orientation due to internal fluctuations. Figure 10 shows one of these events (note that we are performing a simulation with a longer transient and larger number of particles). Again, the amplitude equations provide a good picture of the particles' system dynamics (see Fig. 8).

Moreover, the amplitude equations also predict the orbit sizes. In fact, Fig. 11 shows a comparison between the temporal average of $|\mathcal{A}_0|$ (particles' system) and $|A_0|$ (amplitude equations). Both show a good agreement above criticality. Below criticality, the only attractor of the amplitude equations system is the asynchronous state with all the amplitudes nulls. In contrast, the particles' system shows some pattern-forming activity. This might be attributed to the noisy
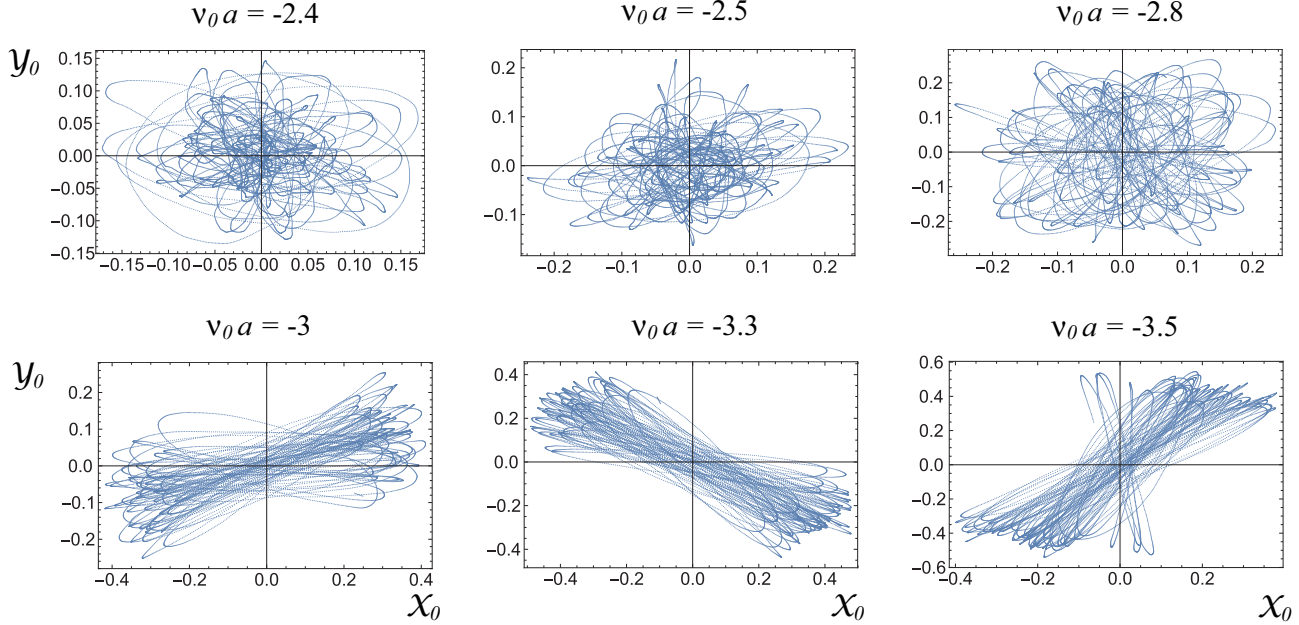
FIG. 9. Numerical simulation of the equations of motion (3) and (4) for $v = 0.001$, $\sigma = 0.1$, $\eta = 0.5$, $N = 1000$, $L_x = 1$, and $dt = 0.05$ (using an Euler-Maruyama method). We are showing $\mathcal{A}_0 = \mathcal{X}_0 + i\mathcal{Y}_0$, as defined in Eq. (27) for different values of $\nu_0 a$. More precisely, we initialize the system with randomly distributed positions and polarizations at $\nu_0 a = -2$, run it for a time $t_0 = 2 \times 10^3$, and collect data for a time $\Delta t = t - t_0 \in [0, 10^3]$. Then, we decrease $\nu_0 a$ in $\delta = -0.1$ and repeat the procedure (run the system for a time $t_0 = 2 \times 10^3$ and collect data for a time $\Delta t = t - t_0 \in [0, 10^3]$). We did it up to $\nu_0 a = -3.5$.

precursor of the pattern [31]. If this is the case, it is possible to claim that the waves appear via a supercritical transition.

B. Discrepancies

Figure 12 shows $|\mathcal{A}_+|$ versus $|\mathcal{A}_0|$; $|\mathcal{A}_-|$ versus $|\mathcal{A}_0|$ displays the same pattern. The thin curves correspond to particles' system simulations (same numerical data as in Fig. 10). The amplitudes $|\mathcal{A}_\pm|$ and $|\mathcal{A}_0|$ are following down in a very synchronous way. That is, they are alternating between zero and their maximum values. This means that the maximum level of anti-aligning synchrony is reached when the standing wave is almost flat ($|\mathcal{A}_0|$ is almost zero), namely, when the particles are scattered along the channel. On the other hand, when the standing wave reaches its maximum amplitude, the

particles' polarizations are completely disordered ($|\mathcal{A}_\pm|$ is almost zero).

The dotted structure of Fig. 12 is obtained from numerical simulations of the amplitude equations. They are missing the following down of the $|A_\pm|$ amplitudes. In contrast, they predict that $A_\pm$ will be orbiting around the unstable fixed point (21). Appendix B presents more details about the $A_\pm$ orbits. The thick line in Fig. 12 shows the module of this unstable solution. Therefore, the amplitude equations approach is still a good predictor of the maximum values reached by $|\mathcal{A}_\pm|$. However, since they are missing the following downs, the temporal averaging of these amplitudes is overestimated. Of course, we may attribute the $|\mathcal{A}_\pm|$ following downs to the internal fluctuations of the particles' system. The synchronization between the $|\mathcal{A}_\pm|$ and $|\mathcal{A}_0|$ following downs, however, seems more than simple noise. The noisy correction to the nonlinear
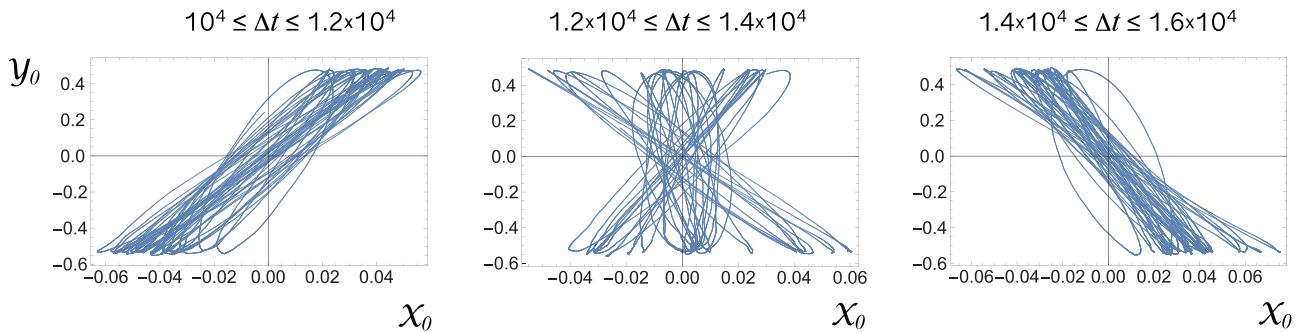

FIG. 10. Numerical simulation of the equations of motion (3) and (4) for $\nu_0 a = -3$ and $N = 3500$ (other parameters as in Fig. 9). The different panels show $\mathcal{A}_0 = \mathcal{X}_0 + i\mathcal{Y}_0$, as defined in Eq. (27), at different times windows of $\Delta t = t - t_0$, with $t_0 = 5 \times 10^4$.
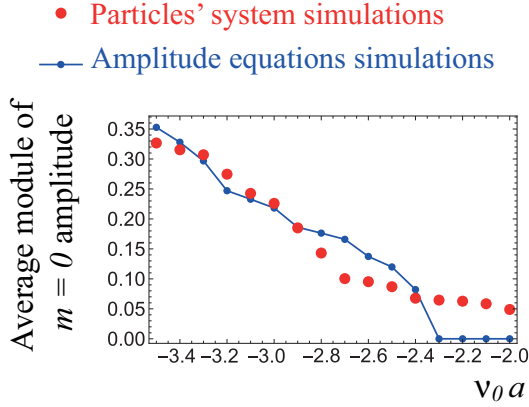
● Particles' system simulations

━●━ Amplitude equations simulations

FIG. 11. Comparison between the temporal average of $|\mathcal{A}_0|$ (particles' system) and $|A_0|$ (amplitude equations). We use the same numerical data as Fig. 9 for the particles' system. We reproduce the experiment with the amplitude equations (13)–(15) [30], dropping a longer transient $t_0 = 2 \times 10^4$.

Fokker-Planck equation (6) is multiplicative [12,32]. Perhaps it is a constructive effect of multiplicative noise. If such conjecture is correct, this discrepancy is expected to persist for a larger number of particles. In fact, mean-field approaches such as Eq. (6) take first the limit $N \to \infty$, and then $t \to \infty$. The opposite choice, first $t \to \infty$, and then $N \to \infty$, does not necessarily commute with the former. Consequently, although multiplicative fluctuations decay as $N^{-1/2}$, they might leave a mark in the nonequilibrium steady state even at the thermodynamic limit.

V. SUMMARY AND FUTURE PROSPECTS

We have proposed a quasi-one-dimensional simplification of the model presented in Ref. [23], namely, anti-aligning active particles confined in a thin channel. This system exhibits a finite wavelength instability as well as the two-dimensional model of Ref. [23]. The instability leads to the
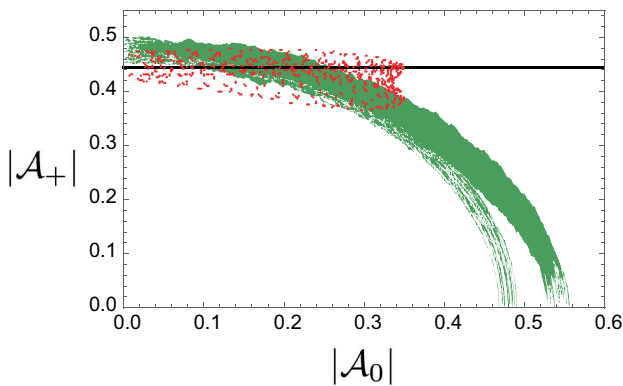

FIG. 12. $|\mathcal{A}_+|$ versus $|\mathcal{A}_0|$. The thin curves correspond to numerical simulations of the equations of motion (3) and (4), where we are using the same numerical data used in Fig. 10. Dots correspond to numerical simulations of the amplitude equations (13)–(15) [30]. The thick line corresponds to the module of the unstable solution (21), that is, $\sqrt{\varepsilon/3c_3}$.

formation of a longitudinal density wave. To wit, a standing wave composed of two counterpropagating traveling waves.

Of course, this wave is a dissipative structure whose spatiotemporal dynamics is ruled by attractors. Neglecting the inherent fluctuations of the system, near criticality, and for low speed, we have deduced a set of amplitude equations that govern this dynamics. These equations have chaotic attractors.

We have compared the dynamics predicted by the amplitude equations with direct numerical simulations of the particles' system. The amplitude equations approach captures the waving behaviors of the particles' density along the channel well. The agreement is qualitatively and quantitatively good, being near criticality and having low speed. However, the amplitude equations fail to predict the follow-down of the anti-aligning synchrony when the standing wave reaches its maximum amplitude. We have conjectured that it might be attributed to the presence of multiplicative noise in the macroscopic variables.

Therefore, the inclusion of the fluctuating term into Eq. (6) [12,32] and the computation of the stochastic normal form should be addressed in future investigations.

Furthermore, the presence of chaotic orbits in this quasi-one-dimensional reduction supports the conjecture that the dynamics of dancing hexagons also exhibit chaos [23]. Of course, a complete study of two-dimensional waves must also be addressed in future works. It is worth mentioning that turbulence seems to be relevant in this kind of active system. For instance, Großmann *et al.* reported mesoscale turbulence in a closely related system of active particles [25].

APPENDIX A: AMPLITUDE EQUATIONS DERIVATION

Let us introduce the inner product

$$\langle \phi \,|\, \psi \rangle = \frac{1}{2\pi L_x} \int_0^{2\pi} d\theta \int_0^{L_x} dx \phi^* \psi,$$

and the Dirac notation

$$\exp\left\{ i\left(\frac{2\pi n}{L_x} x + m\theta \right) \right\} = |nm\rangle,$$

where, according to the periodic boundary conditions, $|n\,m\rangle$ is a complete basis of the functional space, with

$$\langle nm|n'm'\rangle = \delta_{n,n'}\delta_{m,m'}.$$

Then, we rewrite the probability $P(\theta, x, t)$ in terms of the deviation to the asynchronous state

$$P(\theta, x, t) = \frac{1}{2\pi L_x}(1 + \delta P(\theta, x, t)),$$

thus, Eq. (6) takes the form

$$\partial_t \delta P = (\mathcal{L}_C + \delta \mathcal{L})\delta P - \partial_\theta[\delta P \mathcal{T}_x \delta P], \qquad \text{(A1)}$$

where

$$\mathcal{L}_C = \sum_{n=-\infty}^{\infty} \sum_{m=-\infty}^{\infty} \lambda_{nm}^C |nm\rangle\langle nm|,$$

with

$$\lambda_{nm}^C = -\frac{\eta}{2}m^2 + \frac{v_0 a_c}{2}\left(\frac{\sin\left(2\pi n\sigma/L_x\right)}{2\pi n\sigma/L_x\sigma}\right)(\delta_{m,1} + \delta_{m,-1}),$$

that is, λ_{nm}^C corresponds to $\lambda_m^{[0]}(k)$ at the critical point a_c. Therefore,

$$\ker\left[\mathcal{L}_C\right] = \{|n_c \ -1\rangle, |n_c \ 0\rangle, |n_c \ 1\rangle,$$
$$\times |-n_c \ -1\rangle, |-n_c \ 0\rangle, |-n_c \ 1\rangle\},$$

$$\delta\mathcal{L} = \varepsilon\Delta\mathcal{L}_0 + v\mathcal{L}_1,$$

where

$$\Delta\mathcal{L}_0 = \sum_{n=-\infty}^{\infty} |n \ -1\rangle\langle n \ -1| + |n \ 1\rangle\langle n \ 1|,$$

$$\varepsilon = \frac{\eta(a - a_c)}{2a_c},$$

and

$$\mathcal{L}_1 = \frac{i\pi\sigma}{L_x}\sum_{n=-\infty}^{\infty}\sum_{m=-\infty}^{\infty} n(|n \ m+1\rangle\langle n \ m| + |n \ m-1\rangle\langle n \ m|),$$

$$\mathcal{T}_x = \frac{v_0 a_c}{2i}\sum_{n=-\infty}^{\infty}\left(\frac{\sin\left(2\pi n\sigma/L_x\right)}{2\pi n\sigma/L_x\sigma}\right)(|n \ -1\rangle\langle n \ -1|$$
$$+ |n \ 1\rangle\langle n \ 1|).$$

Now, we will take as small perturbation parameter $|\varepsilon| \ll 1$ (that is, we are near the onset of the instability), with

$$v \sim \varepsilon,$$

and expand

$$\delta P(\theta, x, t) = \sum_{z=1}^{\infty} p^{[z]}(\theta, x, \varepsilon t),$$

where

$$p^{[z]}(\theta, x, \varepsilon t) \sim |\varepsilon|^{z/2}.$$

Notice that we are assuming that $p^{[z]}$ evolves with the slow timescale εt. That is, we are neglecting fast transients that are related to fast-decaying modes and keeping the slow dynamics related to the critical modes that become unstable when $\varepsilon > 0$. Thus,

$$\partial_t p^{[z]} \sim |\varepsilon|^{1+z/2}.$$

Introducing this expansion into Eq. (A1), the first order gives

$$\mathcal{L}_C p^{[1]} = 0,$$

therefore,

$$p^{[1]} = A_+|n_c \ 1\rangle + A_0|n_c \ 0\rangle + A_-|n_c \ -1\rangle$$
$$+ A_+^*|-n_c \ -1\rangle + A_0^*|-n_c \ 0\rangle + A_-^*|-n_c \ 1\rangle.$$

Note that

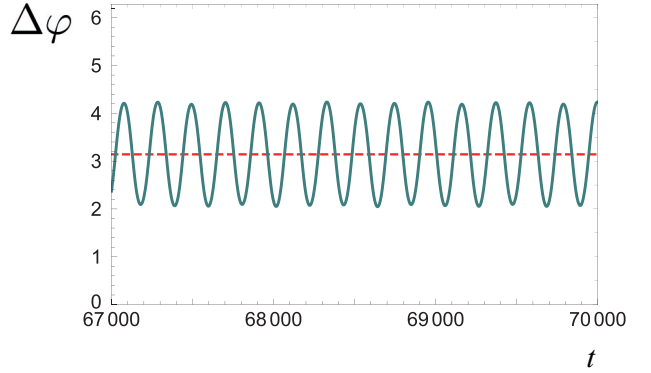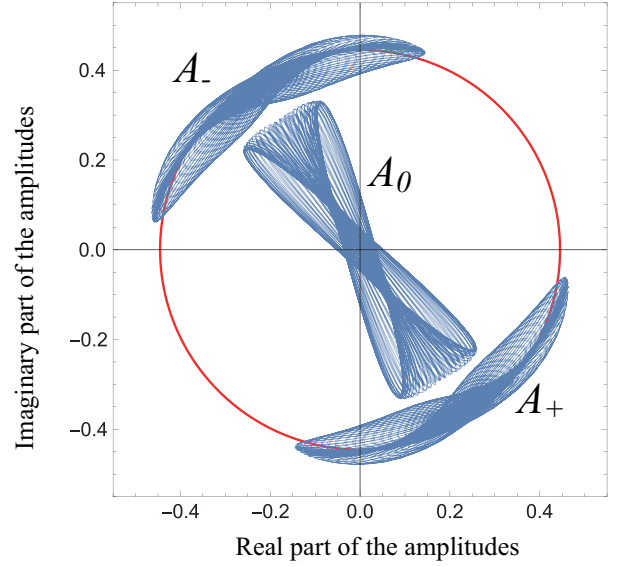$$\dot{A}_\pm \sim \dot{A}_0 \sim |\varepsilon|^{3/2}.$$

FIG. 13. Top: Same as Fig. 5, but we are showing all the amplitudes in the time window $t \in [4 \times 10^4, 7 \times 10^4]$. The thicker circle has a radius corresponding to the module of the unstable fixed point (21), that is, $\sqrt{\varepsilon/3c_3}$. Bottom: Phase shift as defined in Eq. (B1), the dashed line corresponds to the value π.
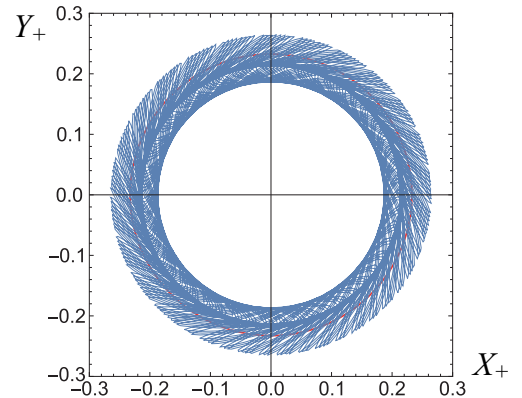

FIG. 14. Same as Fig. 4, but we are showing the amplitude A_+ in the time window $t \in [3 \times 10^4, 7 \times 10^4]$. The thicker circle has a radius corresponding to the module of the unstable fixed point (21), that is, $\sqrt{\varepsilon/3c_3}$.
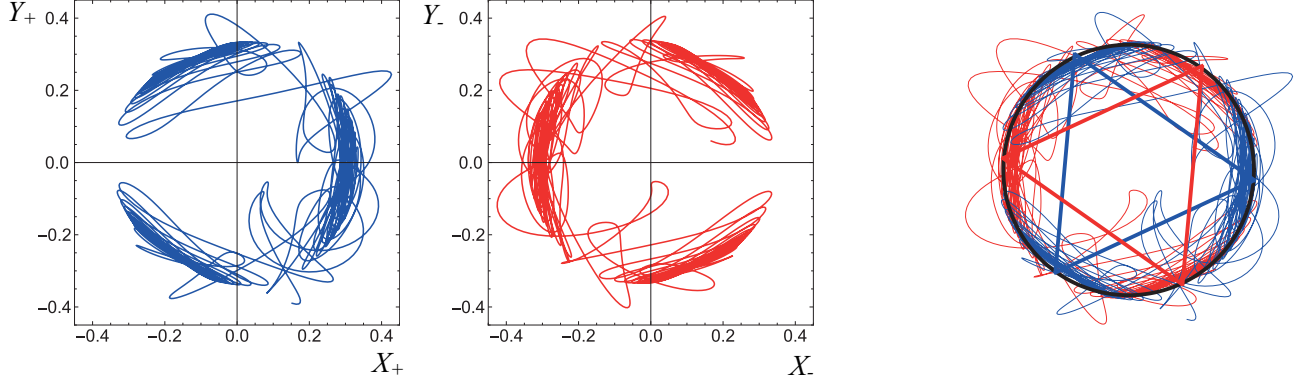
FIG. 15. Numerical simulation of the amplitude equations (13)–(15) [30], for $\varepsilon = 0.04$, we are using the same values of c_1, c_2, and c_3 used the paper, and we have increased the ratio v/L_x by a factor of 8/7 with respect to the simulations shown in Sec. III. Left and middle: $A_\pm$ orbits in the time window $t \in [4 \times 10^4, 5 \times 10^4]$. Right: Both orbits together with the radius $\sqrt{\varepsilon/3c_3}$ circle and two inscribed equilateral triangles, one for each orbit.

The second order gives

$$\mathcal{L}_C p^{[2]} = \partial_\theta [p^{[1]} \mathcal{T}_x p^{[1]}].$$

To solve this equation, its right hand must not contain elements of $\ker[\mathcal{L}_C]$. In this order, it does not, that is,

$$\langle \pm n_c \pm 1 | \partial_\theta [p^{[1]} \mathcal{T}_x p^{[1]}] \rangle = 0,$$

and

$$\langle \pm n_c 0 | \partial_\theta [p^{[1]} \mathcal{T}_x p^{[1]}] \rangle = 0,$$

thus, we can invert the operator $\mathcal{L}_C$, obtaining

$$p^{[2]} = \sum_{n=-\infty}^{\infty} \sum_{m=-\infty}^{\infty} \frac{\langle nm | \partial_\theta [p^{[1]} \mathcal{T}_x p^{[1]}] \rangle}{\lambda_{nm}^C} |nm\rangle.$$

The third order gives

$$\mathcal{L}_C p^{[3]} = (\partial_t - \delta\mathcal{L}) p^{[1]} \\ + \partial_\theta [p^{[1]} \mathcal{T}_x p^{[2]}] + \partial_\theta [p^{[2]} \mathcal{T}_x p^{[1]}].$$

Unlike the second order, the third order does have solvability problems. Here, we must impose solvability conditions in the form

$$\text{if} \quad \psi \in \ker[\mathcal{L}_C] \quad \text{then}$$
$$\langle \psi | (\partial_t - \delta\mathcal{L}) p^{[1]} + \partial_\theta [p^{[1]} \mathcal{T}_x p^{[2]}] + \partial_\theta [p^{[2]} \mathcal{T}_x p^{[1]}] \rangle = 0,$$

which are the conditions that rule the temporal evolution of the amplitudes A_+, A_0, and A_-. More specifically, the amplitude equations (13)–(15) come from the solvability conditions

$$\dot{A}_\pm = \langle n_c \pm 1 | \delta\mathcal{L} p^{[1]} - \partial_\theta [p^{[1]} \mathcal{T}_x p^{[2]}] - \partial_\theta [p^{[2]} \mathcal{T}_x p^{[1]}] \rangle,$$
$$\dot{A}_0 = \langle n_c 0 | \delta\mathcal{L} p^{[1]} - \partial_\theta [p^{[1]} \mathcal{T}_x p^{[2]}] - \partial_\theta [p^{[2]} \mathcal{T}_x p^{[1]}] \rangle,$$

where, after straightforward calculation, we obtain the coefficients

$$c_1 = \frac{-v_0 a_c}{2 \left(1 - \frac{v_0 a_c}{\eta} \right)}, \tag{A2}$$

$$c_2 = c_1 + \frac{\eta}{2(1 - \sec(2\pi n_c \sigma / L_x))}, \tag{A3}$$

$$c_3 = \frac{\eta}{4}. \tag{A4}$$

APPENDIX B: MODE $m = \pm 1$ AMPLITUDE ORBITS

Figure 13, top panel, shows the complex plane of all the amplitudes related to the attractor shown in Fig. 5. In addition to the bone-shaped structure formed by A_0, the amplitudes $A_\pm$ orbit the extremes of this structure. In fact, they are moving around the unstable solution (21). The thicker circle has a radius corresponding to the module of this fixed point $\sqrt{\varepsilon/3c_3}$. Moreover, they are oscillating around the constraint (22). The bottom panel of Fig. 13 shows the phase shift:

$$\Delta\varphi = \varphi_+ - \varphi_- = \text{Im} \left[\ln \left(\frac{A_+}{A_-} \right) \right]. \tag{B1}$$

Figure 14 shows the A_+-orbit for the circular-shaped attractor shown in Fig. 4. Again, it is moving around the unstable solution (21) (see the thicker circle). The A_- orbit is quite similar, with an oscillatory pattern for the phase shift $\Delta\varphi$.

In all our numerical exploration, we have observed the same behavior. That is, at the attractor, the amplitudes $A_\pm$ always orbit around the unstable fixed point (21). There is a vast variety of ways of visiting this fixed point, as shown in Figs. 13 and 14. Moreover, Fig. 15 shows another example. The amplitudes $A_\pm$ are visiting the fixed point, forming lobules, which are separated by angles of $2\pi/3$. The lobules of each amplitude are intercalated, forming angles of $\pi/3$. This scenario becomes clearer if we inscribe, in the radius $\sqrt{\varepsilon/3c_3}$ circle, two equilateral triangles, one for each amplitude. The right panel of Fig. 15 illustrates this geometry.

[1] T. Vicsek, A. Czirók, E. Ben-Jacob, I. Cohen, and O. Shochet, Phys. Rev. Lett. **75**, 1226 (1995).

[2] G. Grégoire and H. Chaté, Phys. Rev. Lett. **92**, 025702 (2004); M. Nagy, I. Daruka, and T. Vicsek, Physica A **373**, 445 (2007); M. Aldana, V. Dossetti, C. Huepe, V. M. Kenkre, and H. Larralde, Phys. Rev. Lett. **98**, 095702 (2007); H. Chaté, F. Ginelli, G. Grégoire, and F. Raynaud, Phys. Rev. E **77**, 046113 (2008).

[3] A. P. Solon, H. Chaté, and J. Tailleur, Phys. Rev. Lett. **114**, 068101 (2015).

[4] T. Ihle, Phys. Rev. E **83**, 030901(R) (2011); J. Stat. Mech. (2016) 083205.

[5] L. L. Bonilla and C. Trenado, Phys. Rev. E **98**, 062603 (2018).

[6] R. Großmann, L. Schimansky-Geier, and P. Romanczuk, New J. Phys. **14**, 073033 (2012).

[7] Y. Kuramoto, in *International Symposium on Mathematical Problems in Theoretical Physics*, Lecture Notes in Physics, Vol. 39, edited by H. Arakai (Springer, New York, 1975), p. 420; *Chemical Oscillations, Waves and Turbulence* (Springer-Verlag, Berlin, 1984).

[8] A. A. Chepizhko and V. L. Kulinskii, AIP Conf. Proc. **1198**, 25 (2009).

[9] V. L. Kulinskii, V. I. Ratushnaya, A. V. Zvelindovsky, and D. Bedeaux, Europhys. Lett. **71**, 207 (2005); V. I. Ratushnaya, V. L. Kulinskii, and A. V. Zvelindovsky, D. Bedeaux, Physica A **366**, 107 (2006).

[10] A. A. Chepizhko and V. L. Kulinskii, Physica A **389**, 5347 (2010).

[11] F. J. Sevilla, V. Dossetti, and A. Heiblum-Robles, J. Stat. Mech. (2014) P12025; V. Dossetti and F. J. Sevilla, Phys. Rev. Lett. **115**, 058301 (2015).

[12] F. D. C. Farrell, M. C. Marchetti, D. Marenduzzo, and J. Tailleur, Phys. Rev. Lett. **108**, 248101 (2012).

[13] D. Levis, I. Pagonabarraga, and B. Liebchen, Phys. Rev. Res. **1**, 023026 (2019).

[14] P. Degond and S. Motsch, Math. Models Methods Appl. Sci. **18**, 1193 (2008); P. Degond, G. Dimarco, and T. B. Ngoc Mac, *ibid.* **24**, 277 (2014).

[15] N. Kruk, Y. Maistrenko, and H. Koeppl, Phys. Rev. E **98**, 032219 (2018).

[16] R. S. Negi, R. G. Winkler, and G. Gompper, Soft Matter **18**, 6167 (2022); Phys. Rev. Res. **6**, 013118 (2024).

[17] K. P. O'Keeffe, H. Hong, and S. H. Strogatz, Nat. Commun. **8**, 1504 (2017); N. Blum, A. Li, K. O'Keeffe, and O. Kogan, Phys. Rev. E **109**, 014205 (2024); S. Ansarinasab, F. Nazarimehr, G. K. Sar, F. Ghassemi, D. Ghosh, S. Jafari, and M. Perc, Nonlinear Dyn. **112**, 10465 (2024).

[18] D. Escaff and R. Delpiano, Chaos **30**, 083137 (2020).

[19] D. Escaff, R. Toral, C. Van den Broeck, and K. Lindenberg, Chaos **28**, 075507 (2018).

[20] X.-L. Wu and A. Libchaber, Phys. Rev. Lett. **84**, 3017 (2000); G. Grégoire, H. Chaté, and Y. Tu, Physica D **181**, 157 (2003); J. R. Howse, R. A. L. Jones, A. J. Ryan, T. Gough, R. Vafabakhsh, and R. Golestanian, Phys. Rev. Lett. **99**, 048102 (2007); J. Palacci, C. Cottin-Bizonne, C. Ybert, and L. Bocquet, *ibid.* **105**, 088304 (2010); G. Volpe, I. Buttinoni, D. Vogt, H. J. Kummererb, and C. Bechingerab, Soft Matter **7**, 8810 (2011); P. Romanczuk, M. Bar, W. Ebeling, B. Lindner, and L. Schimansky-Geier, Eur. Phys. J. Spec. Top. **202**, 1 (2012); M. E. Cates and J. Tailleur, Europhys. Lett. **101**, 20010 (2013); G. Ramos, M. L. Cordero, and R. Soto, Soft Matter **16**, 1359 (2020); A. Villa-Torrealba, C. Chávez-Raby, P. de Castro, and R. Soto, Phys. Rev. E **101**, 062607 (2020); A. Villa-Torrealba, S. Navia, and R. Soto, *ibid.* **107**, 034605 (2023).

[21] D. Escaff, Chaos **33**, 043137 (2023).

[22] H. R. Brand and R. J. Deissler, Phys. Rev. Lett. **63**, 2801 (1989); M. Bär, M. Eiswirth, H. H. Rotermund, and G. Ertl, *ibid.* **69**, 945 (1992); M. Argentina, P. Coullet, and V. Krinsky, J. Theor. Biol. **205**, 47 (2000); O. Descalzi, J. Cisternas, and H. R. Brand, Phys. Rev. E **74**, 065201(R) (2006); O. Descalzi, J. Cisternas, P. Gutierrez, and H. R. Brand, Eur. Phys. J. Spec. Top. **146**, 63 (2007); O. Descalzi, J. Cisternas, D. Escaff, and H. R. Brand, Phys. Rev. Lett. **102**, 188302 (2009).

[23] D. Escaff, Phys. Rev. E **109**, 024602 (2024).

[24] L. L. Bonilla and C. Trenado, Phys. Rev. E **99**, 012612 (2019).

[25] R. Großmann, L. Schimansky-Geier, and P. Romanczuk, New J. Phys. **15**, 085014 (2013); R. Großmann, P. Romanczuk, M. Bär, and L. Schimansky-Geier, Phys. Rev. Lett. **113**, 258104 (2014); Eur. Phys. J. Spec. Top. **224**, 1325 (2015).

[26] H. Hong and S. H. Strogatz, Phys. Rev. Lett. **106**, 054102 (2011).

[27] D. Escaff, I. L. D. Pinto, and K. Lindenberg, Phys. Rev. E **90**, 052111 (2014).

[28] M. C. Cross and P. C. Hohenberg, Rev. Mod. Phys. **65**, 851 (1993).

[29] Changing $\frac{2J_1(x)}{x} \rightarrow \frac{\sin x}{x}$, accordingly to the change in the interaction domain shape.

[30] In all our simulations of ordinary differential equations, we have used the MATHEMATICA 12.0.0.0 routine NDSolve, with MaxStepSize = 0.005.

[31] C. Jeffries and K. Weisenfeld, Phys. Rev. A **31**, 1077 (1985); M. Wu, G. Ahlers, and D. S. Cannell, Phys. Rev. Lett. **75**, 1743 (1995); G. Agez, C. Szwaj, E. Louvergneaux, and P. Glorieux, Phys. Rev. A **66**, 063805 (2002); G. Agez, M. G. Clerc, and E. Louvergneaux, Phys. Rev. E **77**, 026218 (2008).

[32] D. S. Dean, J. Phys. A: Math. Gen. **29**, L613 (1996).